## *A Two-Species Magneto-Optical Trap Using 39K and 133Cs*

RATKATA, APICHAYAPORN

# A Two-Species Magneto-Optical Trap Using $^{39}$K and $^{133}$Cs

Apichayaporn Ratkata

---

A thesis submitted in fulfilment
of the requirements for the degree of
Master of Science by Research


Department of Physics

Durham University

January 2017

# A Two-Species Magneto-Optical Trap Using $^{39}$K and $^{133}$Cs

Apichayaporn Ratkata

## Abstract

There is great interest in the use of ultracold polar molecules confined in optical lattices for quantum simulation of complex many-body problems. The objective of our work is to realise a system of ultracold fermionic $^{40}$K$^{133}$Cs molecules in a 1D optical lattice consisting of an array of 2D pancake traps. Such a system will enable a wide range of future investigations, including the study of novel regimes of interlayer superfluidity [1]. To create polar molecules we will employ magnetoassociation on an interspecies Feshbach resonance followed by transfer to the rovibrational ground state using STImulated Raman Adiabatic Passage (STIRAP). This thesis reports the progress towards this ambitious goal focusing on the initial laser cooling stage.

We present a simple single cell vacuum system that can be used to locate the interspecies Feshbach resonances essential for magnetoassociation. We give a description of the laser setups for both species, including details of the laser spectroscopy used for frequency stabilisation. We then present results on the optimisation of the magneto optical trap (MOT) for each species (focusing on the most abundant $^{39}$K isotope). The effects of the intensities and detunings of both the cooling and repump light and the magnetic field gradient are investigated in order to maximise the number of trapped atoms. Finally, we present preliminary observations of simultaneously loading overlapped MOTs for both species.

# Declaration

I confirm that no part of the material offered has previously been submitted by myself for a degree in this or any other University. Where material has been generated through joint work, the work of others has been indicated.

Apichayaporn Ratkata
Durham, February 9, 2017

*Dedicated to my family,*
*for everything.*

# Acknowledgements

I would like to thank everyone who have helped me, especially my supervisor Simon Cornish for helping me become more organised and introducing the "Promising five steps to a successful measurement" as well as explaining key physics concepts. Also thanks for giving me an opportunity to widen my horizons in atomic physics at the Les Houches summer school for a month. I must thank all of my colleagues in the KCs lab for answering my questions and teaching me how to use lasers, set-up optics and physics understanding. In particular I would like to thank Ana Rakonjac for helping me with the magnetic apparatus assembly, Matlab, and proof reading my thesis. Also, Avinash Kumar has helped me in the MOT setup and explained to me the laser locking concept. Danielle Boddy has conjured a thoughtful plan of the optics set-up, built the Cs laser system and importantly proofread my thesis. My thanks also go to Shengkun Fu who is my buddy of taking measurement for a quick setup to the K laser system and Prosenjit Majumder for optimising the K laser stability. I have to thank everyone in the labs in Cornish's group: Steve Hopkins, Alexander Guttridge, Philip Gregory, and Oliver Wales for suggestion in the experiment and enjoying the cake club together.
The AtMol group have provided a supportive atmosphere to work, especially my fellows of graduate class of 2016, that I have gained not only knowledge but also an amusement. I am grateful for the staff of the department, those in financial and administrative support and in the mechanical and electronic workshops, who are friendly to help and be part of my lab progress.
Finally, the largest thanks must go to my dad, my mom and my sister for their love and emotional support that makes me little struggle from being far apart across a continent.

# Contents


Page

**Abstract** **i**

**Declaration** **ii**

**Acknowledgements** **iv**

**Contents** **v**

**1 Introduction** **1**
- 1.1 Motivation . . . 1
- 1.2 Why Ultracold molecules? . . . 2
- 1.3 Why KCs? . . . 2
- 1.4 Objectives and scope . . . 3
- 1.5 How do we make ultracold polar molecules? . . . 4
  - 1.5.1 Laser cooling and trapping . . . 5
  - 1.5.2 Evaporative cooling . . . 11
  - 1.5.3 Magneto-association . . . 15
  - 1.5.4 STImulated Raman Adiabatic Passage (STIRAP) . . . 15

**2 Experimental Setup** **17**
- 2.1 Vacuum system . . . 17
- 2.2 Laser system . . . 20
  - 2.2.1 Caesium . . . 20
  - 2.2.2 Potassium . . . 22
- 2.3 MOT setup . . . 23
- 2.4 Magnetic trap . . . 25
- 2.5 Fluorescence imaging for diagnostics . . . 28

**3 Results and Discussions** **32**
- 3.1 Cs Optimisation . . . 33
- 3.2 K Optimisation . . . 35

**4 Conclusions and outlook** **39**
- 4.1 Summary . . . 39
- 4.2 Project Outlook . . . 40

**Bibliography** **42**

# Chapter 1

# Introduction

## 1.1 Motivation

Ultracold gases offer the possibility to research a wide range of fundamental applications such as ultracold chemistry [2], many-body physics [3], precision measurement [4] and quantum simulation [5]. Our research focuses on quantum simulation of many-body problems. The control with which we can manipulate ultracold gases allows us to engineer and simulate simple models in condensed matter physics [6], e.g., spin model in optical lattices [7], and quantum magnetism [8]. Additionally, we can also explore many-body phenomenon such as the superfluid-Mott-insulator quantum phase transition [9], and the BEC-BCS crossover using Fermi condensates [10]. The prospect of achieving bosonic and fermionic degeneracy of ultracold dilute gases is suited to manifest less complicated systems and investigate new phenomena because of the capability to control over their internal degree of freedom. One can essentially transform a Hamiltonian of an interacting physical system into a simpler Hamiltonian associated with atoms, ions and molecules, that can be used as samples to simulate such system. Then by measuring their quantum states, one can elucidate mechanisms underlying the more complex physical phenomenon.

## 1.2 Why Ultracold molecules?

Ultracold polar molecules provide a promising platform to explore condensed matter systems thanks to their long range anisotropic dipole-dipole interaction. For a polarised dipolar gas, in which all electric dipole moments point in the same direction, the energy due to the dipole-dipole interaction, $V_{\mathrm{dd}}$, is given by [11]:

$$V_{\mathrm{dd}} = \frac{C_{\mathrm{dd}}}{4\pi}\frac{(1-3\cos^2\theta)}{r^3}, \tag{1.1}$$

where $r$ is the interparticle distance and $\theta$ is the angle between the interatomic separation and the dipole orientation varying from 0 to $2\pi$. The factor $1/r^3$ exhibits the long range character of the dipole-dipole interaction. The constant $C_{\mathrm{dd}}$ is $d^2/\epsilon_0$ for particles with permanent electric dipole moment $d$ and $\epsilon_0$ is the permittivity of vacuum.

Our ultimate goal is to realise ultracold fermionic polar $^{40}\mathrm{K}^{133}\mathrm{Cs}$ molecules in an array of two-dimensional pancake traps effectively obtained from a one-dimensional optical lattice as demonstrated in fig 1.1. This configuration is suitable to investigate many physical phenomenon, for example, within a single pancake layer topological superfluid phases can be realised, which is a promising candidate for quantum information processing [12]. By applying an external electric field and dressing with a microwave field it offers tunable intermolecular attractive dipole-dipole interactions resulting in superfluid pairing as well as suppression of two-body inelastic losses through chemical reactions. Furthermore, a system of heteronuclear molecules in optical lattices enables interlayer superfluid formation [3]. When considering multilayers, Cooper pairs can be formed between layers; thereby one can also explore the BEC-BCS crossover [1, 3].

## 1.3 Why KCs?

There are many feasible bi-alkali polar molecules that are of interest and have been successfully studied in laboratory such as RbCs [13] and KRb [14]. Ultracold KCs molecules are interesting to explore because of three key

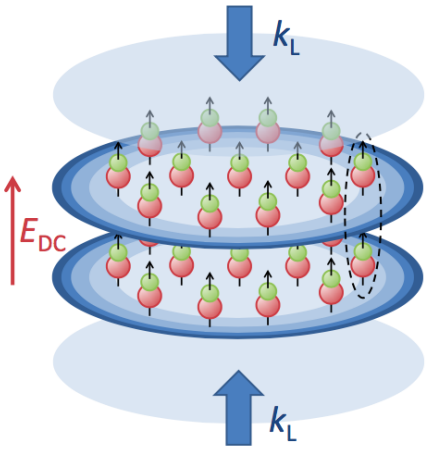


Figure 1.1: Ultracold fermionic $^{40}K^{133}Cs$ molecules confined in a one-dimensional optical lattice of two-dimensional pancake traps. The green spheres represent $^{40}K$ and the red spheres represent $^{133}Cs$. The trap is constructed by interfering two counter-propagating laser beam having identical wavevector $\mathbf{k}_L$. The dipole moments of the molecules are aligned by applying an external electric field $E_{DC}$. Such a system may be used to explore a bilayer superfluidity which the dashed line represents an interlayer Cooper pair.

features. First of all, KCs molecules can be produced as both bosonic and fermionic molecules owing to the existence of three stable potassium isotopes in nature: two bosonic $^{39}K$ (93.258 %); $^{41}K$ (6.730 %); and one fermionic isotope $^{40}K$ (0.012%) [15]. Secondly, they have a permanent dipole moment of 1.906 Debye. More importantly, they are stable against reactive collisions, leading to low trap losses. In other words, the reaction $2KCs \rightarrow K_2 + Cs_2$ cannot take place when there is collision between a pair of KCs molecules.

## 1.4 Objectives and scope

Our specific objectives are to perform interspecies Feshbach resonance spectroscopy for all K isotopes and compare to theoretical predictions by the group of J. Hutson [16]. As bosonic isotopes $^{39}K$ and $^{41}K$ have the highest abundance, we will first focus on identifying the spectrum of interspecies Feshbach resonances of $^{39}KCs$. In order to do this, we must develop the vacuum chamber and laser systems necessary for the production of ultracold mixtures of K and Cs. To measure the Feshbach spectrum, we have developed a simple

single-cell chamber based upon the design described in [17], and briefly described in section 2.1. Pre-cooling a large number of both species is essential before other cooling stages, i.e., magnetic trapping and evaporative cooling. The laser cooling and trapping technique we use is a magneto-optical trap (MOT). Therefore, this dissertation mainly contains theoretical background (chapter 1), MOT setup (chapter 2) and MOT optimisation (chapter 3 ) to maximise the collection of atomic clouds of both species: $^{39}$K and $^{133}$Cs individually. We discuss in chapter 4 an outlook for the experiment and the prospect of trapping single KCs molecules in an optical tweezer.

## 1.5 How do we make ultracold polar molecules?

There are two routes to make cold molecules: a direct; and an indirect approach [18]. The first method to make molecules relies on directly cooling stable molecules. Owing to complex energy level structure, which the molecules in the excited state can possibly decay to various vibrational ground state, it is challenging to determine the cyclic cooling transition. Moreover, samples are difficult to cool to a high phase-space density. Nevertheless, several experimental techniques to cool molecules have been successfully developed; for instance, Stark deceleration [19]; sympathetic cooling [20]; laser cooling [21, 22]; and buffer gas cooling [23]. The second, indirect method to make molecules starts from preparing ultracold atoms at a high phase-space density (PSD) and then associating them to form diatomic molecules via photoassociation [24] or magneto-asso ciation [2]. In our experiment we intend to exploit the latter, indirect, technique to make ultracold KCs molecules.

In this section, we will describe the experimental techniques in general for the production of degenerate quantum gases followed by the ground state molecules formation. There are mainly two stages for producing degenerate ultracold atoms: laser-cooling and trapping, in particular using magneto-optical trap (MOT), and evaporative cooling.

Once quantum degenerate gases of two species is achieved, weakly bound molecules are created by ramping the magnetic field. Theses molecules can

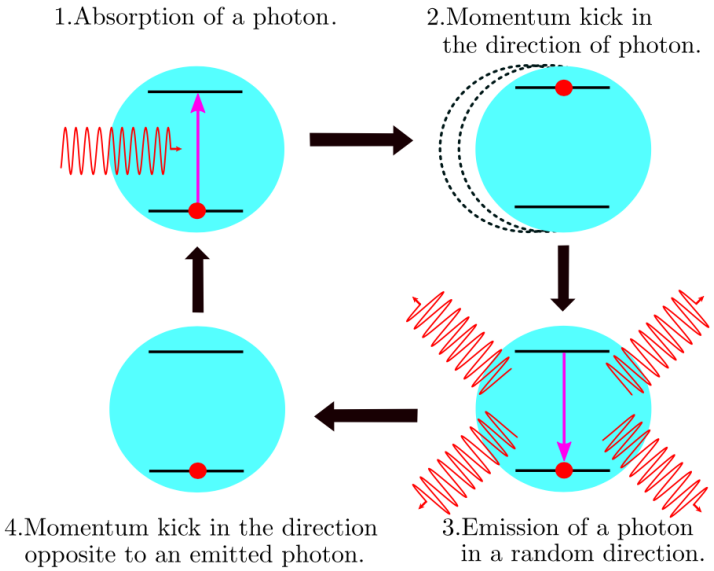


Figure 1.2: The mechanism of how an atom is decelerated by the radiation pressure force from light. An atom absorbs a photon and is jumped to an excited state shown in (1). To preserve the total momentum of the system, the atom recoils in the direction of the incoming photon shown in (2). Momentum change causes a force exerting on the atom. Thanks to a short lifetime of the excited state, the atom spontaneously decays to its initial state and simultaneously emit the photon shown in (3). As the matter of fact that the photon is emitted in a random direction, the momentum kick obtained from many spontaneous emission processes average to zero. This is the cyclic process of momentum transfer and the atom is eventually slowed down. (Figure adapted from [26]).

then be transferred into the lowest rovibrational ground state via STImulated Raman Adiabatic Passage (STIRAP) [25].

### 1.5.1 Laser cooling and trapping

The mechanism underlying laser cooling is an atom-light interaction used to cool down an ensemble of atoms. It can be understood by the semi-classical approach where an atom, a quantum mechanical two-level object, interacts with the classical coherent field. Consider a total system of one atom and one photon as shown in fig 1.2. Each time the atom absorbs (or emits) a photon, the internal energy of the atom has changed jumping from the ground state to the excited state due to the conservation of energy. Furthermore, to preserve

the momentum of the system the atomic velocity changes by recoil speed in the direction of light propagation. The recoil velocity originating from the photon's momentum can be determined as: $v_{\mathrm{rec}} = h/\lambda M$, where $h$ is the Planck's constant, $\lambda$ is the wavelength of the laser, and $M$ is the atomic mass. This momentum transfer creates a force exerted on the atoms in the direction of the laser beam. Thanks to a finite lifetime of the excited state, the atom spontaneously decays back to the initial state and the photon is emitted in a random direction together with atomic recoil against it. Over many absorption and emission cycles there is no net force from the emission process and therefore the mean radiation pressure force from the laser with wavevector $\mathbf{k}_{\mathrm{L}}$, frequency $\omega$ and intensity $I$ exerts a force on the atom in the same direction as the laser beam given by:

$$\mathbf{F}_{\mathrm{pr}}(I,\Delta) = \hbar\mathbf{k}_{\mathrm{L}}\frac{\Gamma}{2}\frac{\frac{I}{I_{\mathrm{sat}}}}{1+\frac{I}{I_{\mathrm{sat}}}+\frac{4\Delta^2}{\Gamma^2}}, \tag{1.2}$$

where $\Delta = \omega - \omega_0$, $\Gamma$ is the natural linewidth of the excited state thus the inverse of its lifetime, $I_{\mathrm{sat}}$ is transition saturation intensity and $\hbar = h/2\pi$, which $h$ is the Planck's constant. It vitally implies that the atom at rest will remain at rest because there is no net force acting on it. However, in reality the atoms moves with velocity $\mathbf{v}$; as a result, the Doppler effect has to be taken into account and will be discussed in sec 1.5.1. Therefore, atoms with different velocities seeing different frequencies of the light, leads to non-zero radiation pressure force exerting on them.

### Doppler cooling

Consider a situation in one dimension as shown in fig 1.3: an atom with velocity $\mathbf{v}$ is exposed to two counter-propagating laser beam having the same angular frequency $\omega$ and whose wavevectors $\mathbf{k}_{\mathrm{L}}$ align along the atomic motion. According to the Doppler effect, in the atomic rest frame the atom sees the laser frequencies shifted up (or shifted down) for the counter-propagating (or co-propagating) beam, resulting in a force imbalance. Atoms can be decelerated if they interact with a red-detuned laser beam, where its frequency is slightly below resonance, on the order of the natural linewidth (typically

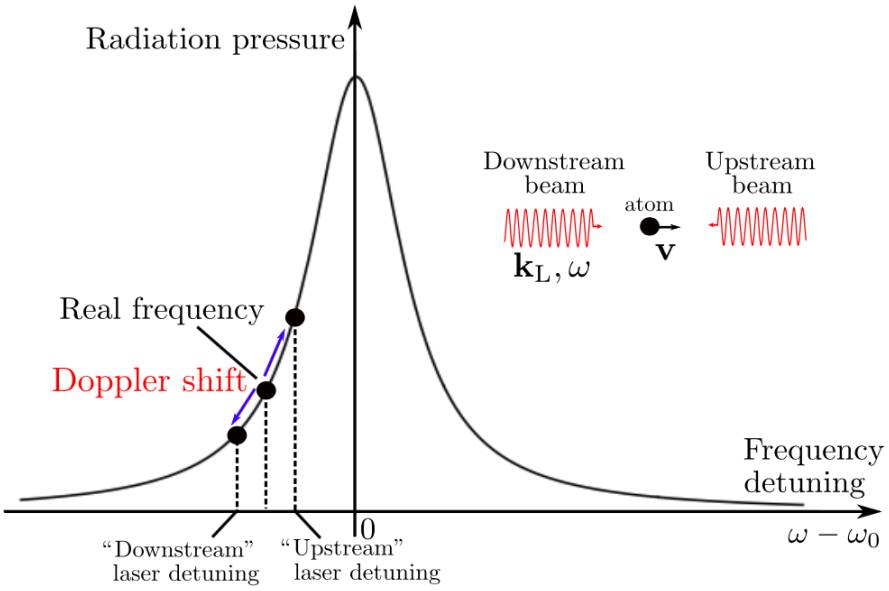


Figure 1.3: Illustration of Doppler cooling in one dimension. Radiation pressure as a function of frequency detuning ($\omega - \omega_0$, where $\omega$ is the laser frequency and $\omega_0$ is the atomic resonance frequency) is illustrated. An atom with non-zero velocity $\mathbf{v}$ encounters the shifted up (down) frequency of the counter (co)-propagating beam in its rest frame. As a consequence, there are force imbalances acting on the atom if both beams have the same frequency. In this case, the real frequency is red-detuned from resonance thereby the higher restoring forces from the upstream beam push the atom against the direction of travel. [27]

several MHz). However, there is the force fluctuation thanks to the stochastic nature of spontaneous emission and the laser intensity fluctuation. This leads to heating in the system. As a result, in thermal equilibrium, where the cooling rate is equal to the heating rate, the atomic ensemble can be cooled to a limited finite temperature, named the Doppler temperature ($T_D$) which is expressed as $k_B T_D = \hbar\Gamma/2$. This mechanism is the basic principle of a magneto-optical trap (MOT) as explained in the next section.

### Magneto-optical trap (MOT)

The Doppler cooling mechanism is generally valid for any arbitrary direction in space, therefore three orthogonal pairs of red-detuned counter-propagating beams creates velocity dependent radiation pressure force on atoms. This

configuration is called optical molasses because a frictional force is exerted on the atoms: this causes the atoms to slow down when they enter a region where all the laser beams intersect. However, atoms can diffuse out of the molasses, which limits the number of pre-cooled atoms, therefore trapping is needed. Aiming to trap atoms at the centre of the trap, the frictional force acting on atoms needs to be spatially-dependent. This can be achieved by adding the quadrupole field, which creates the zero magnetic field at the trap centre and the Zeeman energy shift as a function of position. The field is produced by two current coils in the anti-Helmhotz configuration and characterised by the linear magnetic field gradient.

To understand the principle of the mechanism, we can simply consider a two-level system in one dimension as illustrated in fig 1.4. Note that, the quantisation axis and the polarisation of the light is represented relative to the magnetic field direction. From the diagram the magnetic field breaks the degeneracy of the hyperfine level in which the energy levels are linearly proportional to the magnetic moment quantum number $m_F$ and the magnitude of the magnetic field $|\mathbf{B}|$. Both beams are right-handed circularly polarised light. In the case of red-detuned beams, atoms moving against the direction of the laser beam are more likely to jump into the $m_F = -1$ excited state. In other words, the $\sigma^-$ transition is driven. Eventually, atoms experience the restoring force and are pushed towards the centre of trap where the MOT is collected.

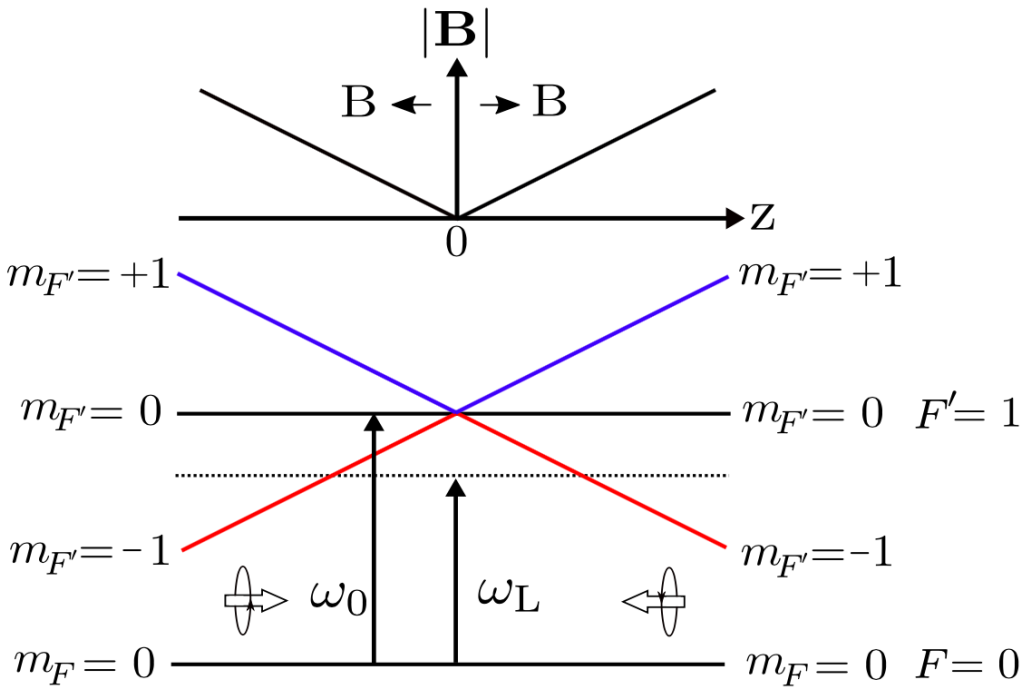


Figure 1.4: Schematic of the principle of a simplified one-dimensional magneto-optical trap (MOT): Energy level splitting of an atom having $F = 0$ ground state and $F' = 1$ excited state in the presence of a linear magnetic field gradient. The magnetic moment quantum number is denoted as $m_F$. The atomic resonance frequency and the laser frequency are represented by $\omega_0$ and $\omega_L$ respectively. The atom interacts with two red-detuned counter-propagating laser beams having the same circularly polarisation. Note that the polarisation is defined according to the direction of the magnetic field, hence the right-handed circular polarised light is shown here. In addition, the magnitude of the quadrupole fields $|\mathbf{B}|$ as a function of position is presented along with arrows indicating the direction of the fields.

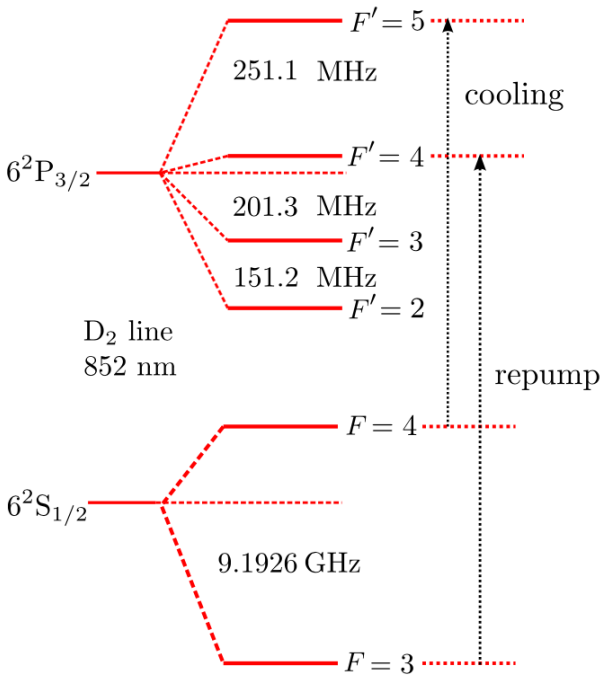


Figure 1.5: Scheme of hyperfine features of $^{133}$Cs energy level. Thanks to selection rules of electric-dipole-allowed transitions, $\Delta F = 0, \pm 1$ as well as a finite linewidth of the excited state, atoms in $F = 4$ can feasibly jump to the excited state $F' = 4$ and spontaneously relax to the $F = 3$ state leading to leaving the cyclic cooling. Therefore, we cool atoms on $F = 4 \rightarrow F' = 5$ and to recycle the atoms out of the $F = 3$ ground state we use repump laser light on $F = 3 \rightarrow F' = 4$. [28]

However, in reality an atom has a multi-level configuration. All the alkali-metal atoms have a hyperfine structure presenting in both ground and excited state on the order of tens or hundreds MHz, for example, the energy level structure of Cs is shown in fig 1.5. Ideally, the cooling transition should be a closed transition, however due to neighbouring open transitions, there is a finite probability that the atom will spontaneously decay to another hyperfine level ground state called the dark state, in which atoms no longer interact with the cooling beam. As a consequence, repump light is required so as to pump atoms back into the cooling cycle. In the case of Cs atom in fig 1.5, the closed transition is $6^2S_{1/2}$ $F = 4 \rightarrow 6^2P_{3/2}$ $F' = 5$ and the repump transition is $6^2S_{1/2}$ $F = 3 \rightarrow 6^2P_{3/2}$ $F' = 4$.

### 1.5.2 Evaporative cooling

Once the pre-cooled atoms are captured in the MOT, they are then transferred to a conservative trap where evaporative cooling can be used to produce colder atoms at a high PSD. The requirement of this technique is the confinement along with long storage time. As a consequence, the use of magnetic traps is introduced. It is typically an inhomogeneous magnetic quadrupole field. In the presence of a magnetic field, the Zeeman $m_F$ energy level is shifted by $g_F m_F \mu_B B(\mathbf{r})$ [11]. According to classical electromagnetic field, in free space only a magnetic field minimum can be produced as a trap and there is no magnetic field maximum [29]. Therefore, trapped atoms have to be in a low-field seeking state associated with the states having $g_F m_F < 0$, which corresponds to being anti-aligned with respect to the magnetic field. To illustrate this, for $^{133}$Cs the magnetically trapped state of $|F = 3, m_F = -3\rangle$ is aimed to be prepared. From MOT loading, this can be achieved by a compressed MOT (cMOT), optical molasses and optical pumping respectively. During the cMOT the atomic density increases and in the optical molasses phase the atoms are further cooled. Once the optical pumping stage is optimised, atoms can be accumulated in the $|F = 3, m_F = -3\rangle$ state ready for magnetic trap loading.

In the magnetic trap, the evaporation is forced by application of energy-selective radiofrequency (RF) that excites trapped states to untrapped states [11]. The spatial Zeeman shift of the atomic energy level occurs thanks to the presence of inhomogeneous magnetic field. The procedure is illustrated in fig 1.6 where the RF is iteratively chosen in such a way that its energy matches the energy separation between the trapped and untrapped states of atoms around the tail of the velocity distribution. In other words, hot atoms are removed towards untrapped states and rethermalisation repeatedly occurs leading to lower temperature of the ensemble. By ramping the magnetic field gradient and simultaneously decreasing the energy of RF photons, cold atoms at high PSD can be successfully prepared.

In the ultracold regime especially during evaporative cooling, atoms mainly interact via collisions whose cross section is largely determined by an s-wave

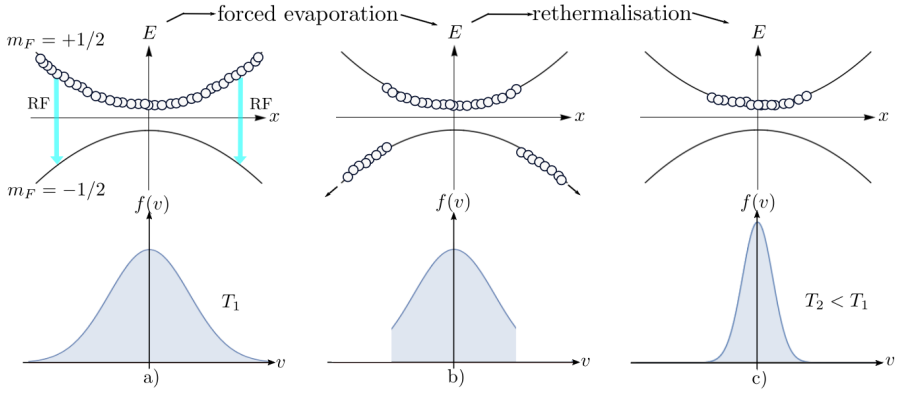


Figure 1.6: RF evaporative cooling is simplified by considering two Zeeman states $m_F = +1/2$ (low-field seeking state/ trapped state) and $m_F = -1/2$ (high-field seeking state/ untrapped state). The top row demonstrates spatial dependence of the potential energy of the atoms, while the bottom ones are corresponding Maxwell-Boltzmann velocity distribution at each stage. The evaporation is forced by selectively exciting the trapped state into the untrapped state via ramping down the RF in which its energy matches the energy difference between two states starting from the tail of the distribution. Subsequently, atoms rethermalise via elastic collisions thereby reaching a lower temperature. (Figure adapted from [11]).

scattering length ($a$), typically expressed in the unit of Bohr's radius, $a_0$, where $a_0 = 0.0529$ nm. As a consequence, the understanding of the scattering length behaviour as well as Feshbach resonances will be critically discussed in the next section. Moreover, this supports why we aim to locate both intraspecies and interspecies Feshbach resonances, as selecting appropriate values of magnetic fields will be able to attain efficient evaporation.

### Scattering length

In neutral ultracold gases, a short-range contact interaction dominates that is described by molecular potentials, an example depicted in fig 1.7(a). This is called the van der Waals (VdW) interaction that is a function of interatomic separation $R$, proportional to $1/R^6$. It has a repulsive feature at zero interatomic separation and an attractive feature at larger distances. An important parameter that quantifies the binary interaction strength is the s-wave scattering length particularly in the near zero energy collision regime. Its signs determine the interaction's character whether it is repulsive corre-

sponding to the positive scattering length or attractive corresponding to the negative scattering length.

Evaporative cooling relies on elastic collisions allowing rethermalisation. However, in a high density inelastic collisions also play a crucial role, especially three-body collisions which result in trap loss. In this mechanism a molecule is formed and the binding energy is converted into kinetic energy of both the molecule and the third atom and all are expelled out of the trap. Quantitatively, the elastic collision rate is proportional to $a^2$ [30], while three-body losses rate scales as $a^4$ [31]. Therefore, the optimal scattering length need to be carefully selected to efficient allow cooling of the atoms, while three-body losses are suppressed, e.g., a window for effective Cs evaporation is between $a_{\mathrm{Cs}}$ $200a_0 - 400a_0$ according to the previous work [32], corresponding to the magnetic field of 22-25 G.

### Feshbach resonances

As mentioned in the previous section each molecular potential is for a particular internal state and when atoms are in the presence of an external magnetic field, the Zeeman shift happens. This leads to the separation of different molecular states as shown in fig 1.7 (a), associated with different angular momentum quantum numbers $(F, m_F)$ of two colliding atoms, often called channels. A Feshbach resonance is a scattering resonance happening when the energy of the molecular bound state in a closed channel is magnetically tuned in such a way that its energy simultaneously equals that of the open channel potential energy. Interestingly, the scattering lengths varies around a Feshbach resonance as a function of the magnetic field $B$ as shown in fig 1.7 (c) and is given by:

$$a(B) = a_{\mathrm{bg}} \left(1 - \frac{\Delta}{B - B_0}\right), \tag{1.3}$$

where $a_{\mathrm{bg}}$ is the background scattering length associated with the open channel, $B_0$ is the magnetic field at the resonance where the scattering length diverges to $\pm\infty$, and $\Delta$ is the resonance width corresponding to the difference between $B_0$ and the magnetic field at zero-crossing ($a = 0$).

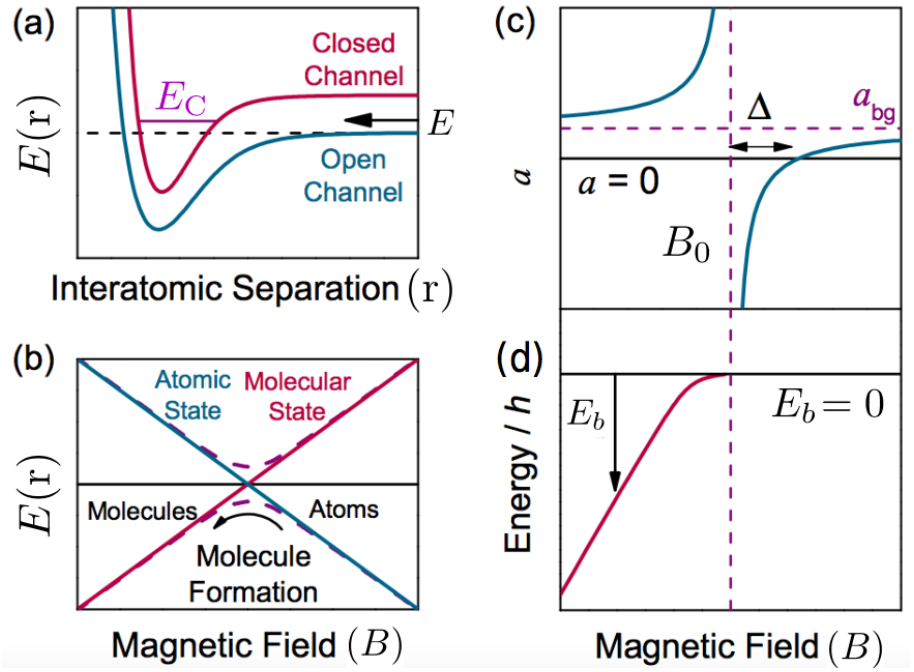


Figure 1.7: (a) An example of molecular potentials $E(\mathrm{r})$. Each channel is associated with the interaction between different hyperfine $m_F$ states of two colliding atoms. A Feshbach resonance occurs when the energy of incoming atom pair ($E$) in the open channel is resonant with the energy of a molecular bound state ($E_\mathrm{C}$) in another channel, denoted as the closed channel. The energy can be controlled by tuning the magnetic field. (b) The avoided crossing between an atomic and molecular state at the Feshbach resonance enable the association of atoms into weakly bound molecules through adiabatically sweeping the magnetic field across from high to low values. (c) The schematic shows the scattering length $a$ in the neighbourhood of the Feshbach resonance as a function of the magnetic fields $B$, where $a_\mathrm{bg}$ is the background scattering length, $B_0$ is the magnetic field at the resonance, and $\Delta$ corresponds to the width between $B_0$ and the magnetic field value at zero scattering length. (d) The bound state with the binding energy $E_b$ with respect to the zero energy of a free atom pair existing at the positive scattering length side of the resonance. (Figure adapted from [33]).

Since exceptionally large scattering lengths enhance both elastic collisions and inelastic collision, we can identify Feshbach resonances location by observing an enhancement of atom losses at some specific magnetic fields.

### 1.5.3 Magneto-association

At a Feshbach resonance, an avoided crossing is formed because of the coupling between a two-free atom colliding state and a weakly bound molecular state. Here we hope to locate interspecies Feshbach resonances in regions of near zero positive background scattering length offering the possibility to create weakly bound polar molecules with low three-body losses [34]. By adiabatically ramping the magnetic fields in fig 1.7(b) from high to low values across the magnetic field at the Feshbach resonance, ultracold degenerate mixtures can be associated into weakly bound heteronuclear molecules [2]. This is an intermediate step to prepare the lowest rovibrational ground state molecules.

### 1.5.4 STImulated Raman Adiabatic Passage (STIRAP)

Feshbach molecules are produced in a very high vibrational excited state, easily undergoing inelastic collision and hence escaping the trap. This is prevented by optically coherent transfer via STIRAP [25] in order to populate the molecules to the lowest rovibrational molecular state. STIRAP is basically a two-photon transition mechanism in a configuration involving two lasers. One couples the weakly bound Feshbach molecular state to an excited state whilst the other couples the excited state to a deeply bound ground state [35]. Eventually, ultracold polar molecules can be further loaded into optical lattices to explore some physical phenomena. In our experiment we aim to load ultracold KCs molecules in a two-dimensional pancake trap. The trap is a one-dimension optical lattice simply formed by two counter-propagating laser beams. Due to their polarisability, the molecules can be trapped at the minima of periodic potentials. Each trap depth can be adjusted by varying the laser intensity. The barriers suppress the collision between molecules at different sites, leading to a stable system and the capability to manipulate

individual molecules.

# Chapter 2

# Experimental Setup

This chapter describes an experimental apparatus designed specifically for the search for interspecies Feshbach resonances of $^{39}K^{133}Cs$ and $^{41}K^{133}Cs$. However, it will be interesting to investigate whether we can use this vacuum system for production of ultracold fermionic rovibrational ground state molecules also. First of all, a brief description of the vacuum system is stated and followed by a description the laser systems for both species in details. Secondly, the MOT optics and sequence are explained, as well as a discussion on the trap and shim coils calibration. Finally, the detection scheme and how to quantify the number of atoms in the MOT are analysed.

## 2.1 Vacuum system

The apparatus is based around a single-chamber, ultra high vacuum (UHV) system maintained by a single ion pump (NEXTorr D100-5 NEG and ion pump). The vacuum assembly is shown in fig 2.1. For a single chamber there are two requirements to balance: the high alkali vapour pressure for initial MOT loading; and subsequent low pressure during evaporative cooling to achieve high phase space density (PSD). We use a dispenser to provide the atomic vapour for the experiment. Previous work in [17] demonstrates that it is possible to modulate the alkali vapour pressure on a 100 ms timescale in a single-chamber system by pulsing the dispensers on and off during the experimental cycle. By designing a dispenser mount that acts as a heat

sink, we can increase the heat transfer rate after the dispenser is switched off. The vapour pressure is manipulated by controlling the current through a computer-controlled power supply.

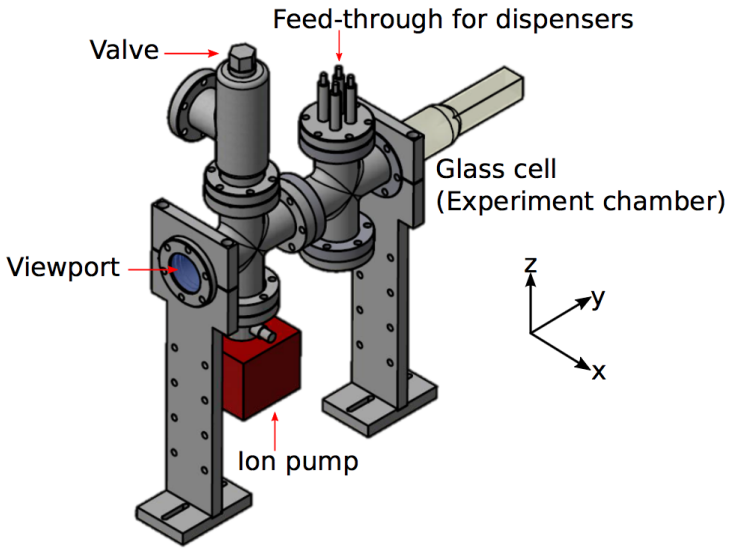


Figure 2.1: Schematic of the vacuum system. The electrical feed-through is used to supply the current to dispensers inside the chamber. The imaging and optical pumping beam will be aligned along y-axis and x-axis respectively.

Our dispenser mount is designed to hold three dispensers: Rb; K; and Cs as shown in fig 2.2. We have included the Rb dispenser because there is a working RbCs molecules experiment in our group that we might use to test our chamber. The K, Cs, and Rb vapour is sourced from commercial dispensers (SAES). As we plan to pulse the dispenser at a high current of around 20 A based on the work in [17], a water-cooling system in fig 2.2 (b) has been added which cools the tip of the electrical feed-through outside the chamber. The water-cooling system consists of four brass blocks labelled A-D as shown in fig 2.2, which are connected to another two brass blocks (E & F) having the water running through. The brass blocks (E & F) are in thermal contact with two thermo-electric cooler (TECs). Also, there is a cross-shaped nylon part hanging in between blocks A to D in order to prevent stress between blocks A-D when we tighten the locking screws (without the nylon cross we risk breaking the electrical feed-through during assembly).

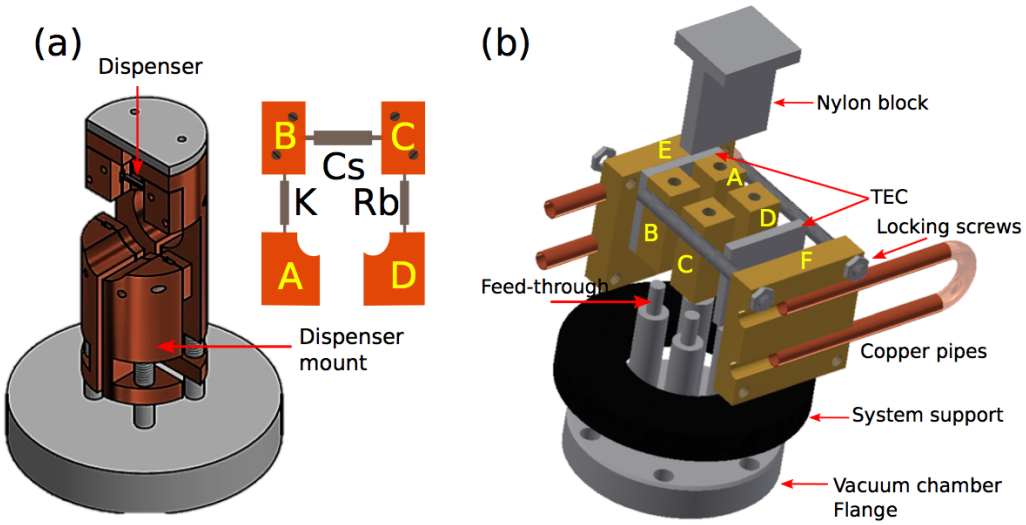


Figure 2.2: (a) The drawing of the copper dispenser mount inside the vacuum chamber. Here, the dispensers are configured in such a way that one power supply can run both K and Cs dispensers. (b) The assembly of a water cooling system. It composes of four brass blocks (A - D) connected to the end of electrical feed-throughs. The next layer is two TECs (depicted in grey) for cooling attached with the E & F brass blocks. Each of these have the copper tubes, which water passes through. All components are in place by locking screws as illustrated in the figure. A nylon block is placed in the middle of side AB and CD to support any compression during assembling, which may crack the feedthroughs.

## 2.2 Laser system

For Cs, the laser system consists of a commercial laser and a home-built laser, which produces the cooling and the repump light, respectively while the K light is all derived from the commercial laser. We use the $D_2$ transition for both Cs and K MOTs. The atomic energy levels on the $D_2$ lines of both $^{133}$Cs and $^{39}$K are shown in figure 2.3. It highlights all transitions needed in the experiment.

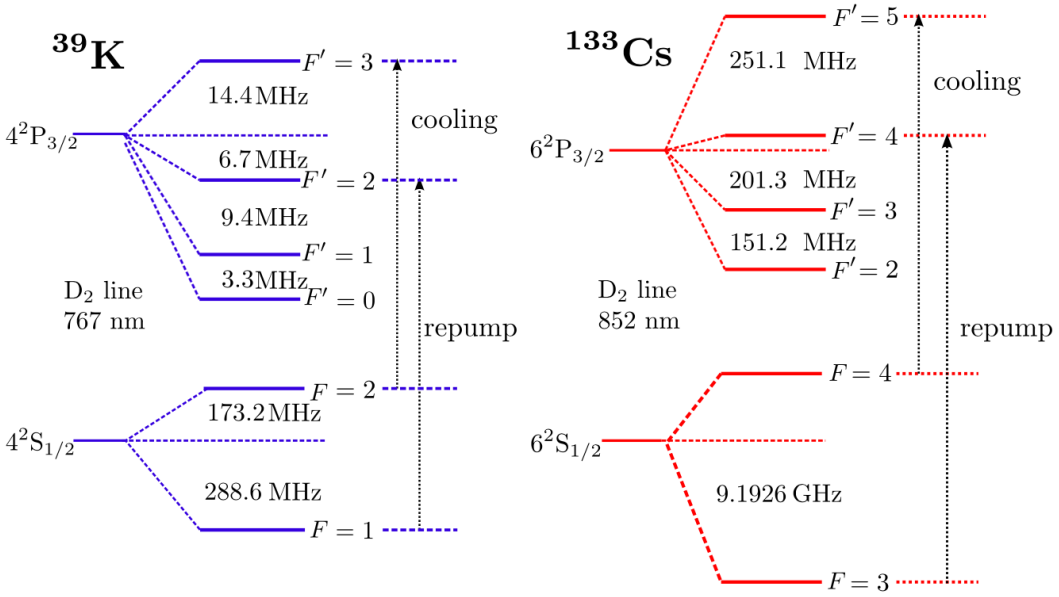


Figure 2.3: Energy level structure of the $D_2$ transition of $^{39}$K and $^{133}$Cs (the diagram is not to scale) [28, 36]. The arrows indicates all transitions needed for cooling and repump in the magneto-optical trap stage.

### 2.2.1 Caesium

The cooling light is provided by a Toptica DL pro laser (100 mW) working at 852 nm operating on the $D_2$ transition $6^2S_{1/2}(F = 4) \rightarrow 6^2P_{3/2}(F' = 5)$. The laser setup is shown in fig 2.4. We stabilise the laser frequency using saturated absorption spectroscopy [37] and the built-in locking electronics. The light used for locking is double-passed through an acousto-optical modulator (Crystal Technology 3110-120), labelled as AOM1 in fig 2.4, so that

we can tune the MOT detuning using AOM1 without misaligning the setup. The laser is locked to the peak of $F' = 4$ and $F' = 5$ crossover resonance as indicated in fig 2.5. The remaining laser light not used in the stabilisation is aligned through a single-pass AOM (AOM2) before being coupled into a fibre splitter. Figure 2.4 shows the optical setup and light paths.

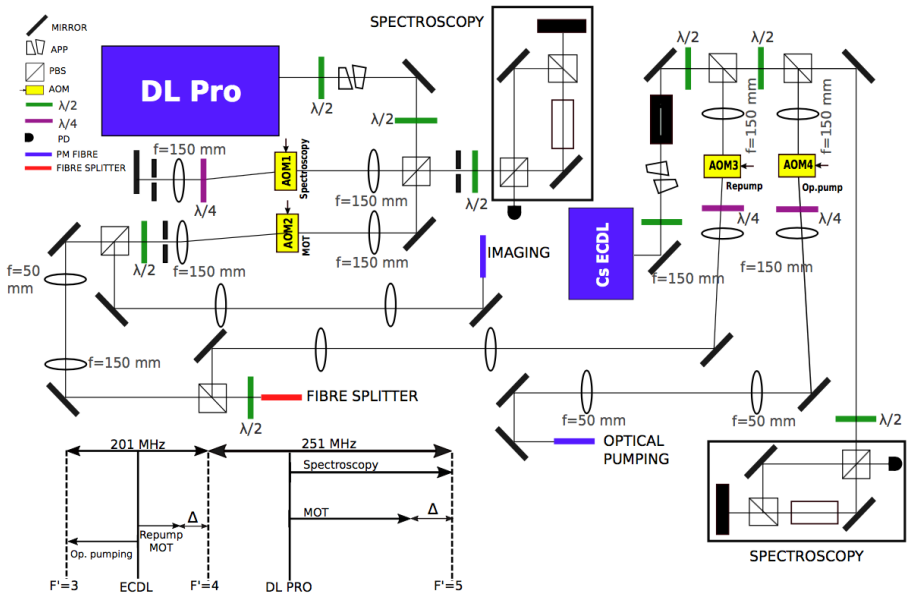


Figure 2.4: Schematic of the Cs laser setup. The cooling light is derived from a Toptica DL Pro and is split into three main paths: spectroscopy; cooling light and imaging light. The repump light is provided by the home-built ECDL laser and is also split into three main paths: spectroscopy, repump light and optical pumping light. The cooling beam is locked to the transition from $F = 4 \rightarrow F' = 5$. The repump beam is locked to $F = 3 \rightarrow F' = 4$ crossover resonance.

The repump light (fig. 2.4) is placed on the same optical table as the cooling light and produced by a home-built external cavity diode laser (ECDL). The light is split into three paths: spectroscopy; MOT repump; and optical pumping light. Although we do not discuss or employ optical pumping light in our experiment during this thesis, we do intend to use it in the near future. The laser is frequency stabilised to $6^2S_{1/2}F = 3 \rightarrow 6^2P_{3/2}F' = 3 : 4$ crossover resonance using saturated absorption spectroscopy (SAS). The stabilisation (locking) scheme we use is a phase-sensitive detection. The SAS signal is sent to a home-built lock box designed by Oxford University, which dithers the laser current to produce an error signal. The output of the photodiode passes

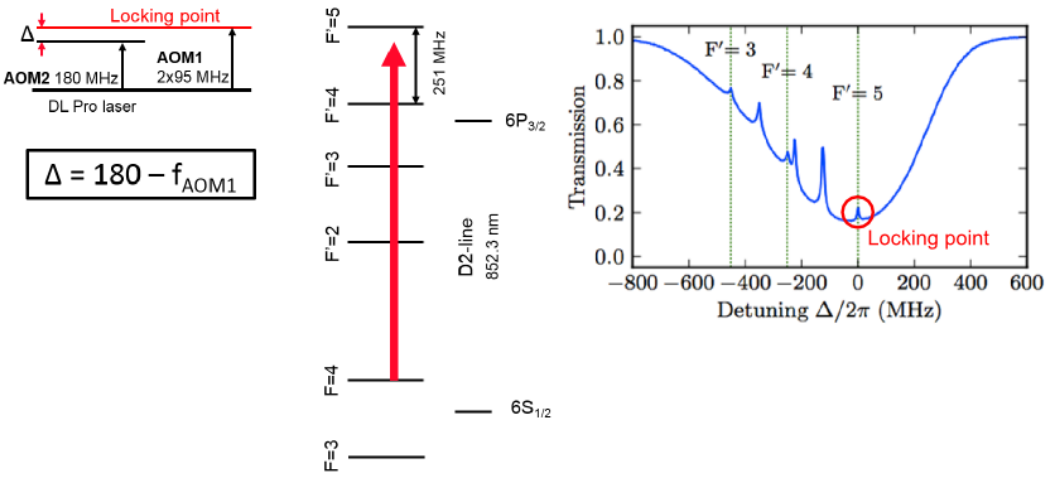


Figure 2.5: Laser locking position of the saturated absorption signal of $^{133}$Cs cooling light together with associated energy levels of the excited state [28].

through a low pass filter to remove the high frequency (dither) component of the signal, which then goes to an integrator PID feedback circuit to correct the laser diode current and piezo.

To tune the repump laser on transition with $6^2S_{1/2}F = 3 \rightarrow 6^2P_{3/2}F' = 4$ transition, the MOT repump light is aligned through a single pass AOM3, as shown in fig 2.4. The MOT repump light is overlapped with the MOT cooling light and aligned down a fibre, which is attached to a one-to-three way splitter. Furthermore, a mechanical shutter is placed in front of the fibre to ensure that no resonant light, which might leak through the AOMs, reaches the atoms during post-MOT stages of the experiment. Note that two lenses before each optical fibre are aligned as a telescope for beam waist matching with the fiber and thus yielding the maximum coupling efficiency.

### 2.2.2 Potassium

The 767 nm light necessary to produce a potassium MOT is generated by a Toptica TA pro laser consisting of a grating-stabilised master laser and a tapered amplifier (TA). There are two output ports: the front port, providing an output power up to 2 W, is responsible for both cooling and repump beams; while the back port produces a 5 mW output, used to lock the laser via modulation transfer spectroscopy (MTS) [38] on the transi-

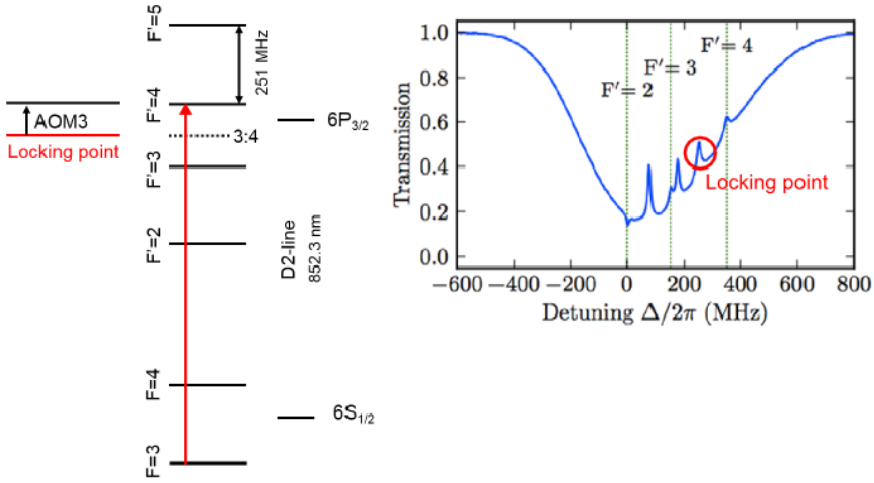


Figure 2.6: Laser locking position of the saturated absorption signal of $^{133}$Cs repump light together with the associated energy levels of the excited state [28].

tion $4^2S_{1/2}F = 2 \rightarrow 4^2P_{3/2}F' = 1, 2, 3$ using the built-in Toptica locking electronics. The setup design in fig 2.7 and 2.8 (a) is able to produce the frequencies suitable for making both $^{39}$K and $^{41}$K MOTs. Since the working frequency of the laser is not exactly resonant with the cooling transition $4^2S_{1/2}(F = 2) \rightarrow 4^2P_{3/2}(F' = 3)$, an AOM is needed to shift the frequency down to resonance frequency labelled as AOM2 in fig 2.7. Additionally, three AOMs are necessarily used to shift the frequency for cooling beam and repump beams of both bosonic isotopes $^{39}$K and $^{41}$K. The laser is locked on the closed transition of $F = 2 \rightarrow F' = 1, 2, 3$ in $^{39}$K. The fig 2.8 (b) indicates the locking point of an error signal (red) produced by MTS together with its associated SAS signal (black).

## 2.3 MOT setup

The setup for both species is basically a six-beam counter-propagating configuration. The cooling and the repump light for each species are combined and transported to the experiment table through a fibre splitter. However, the K MOT light and Cs MOT light are collimated to a different $1/e^2$ radius. The beam waist of Cs light is 3.0(5) mm obtained from the fibre collima-

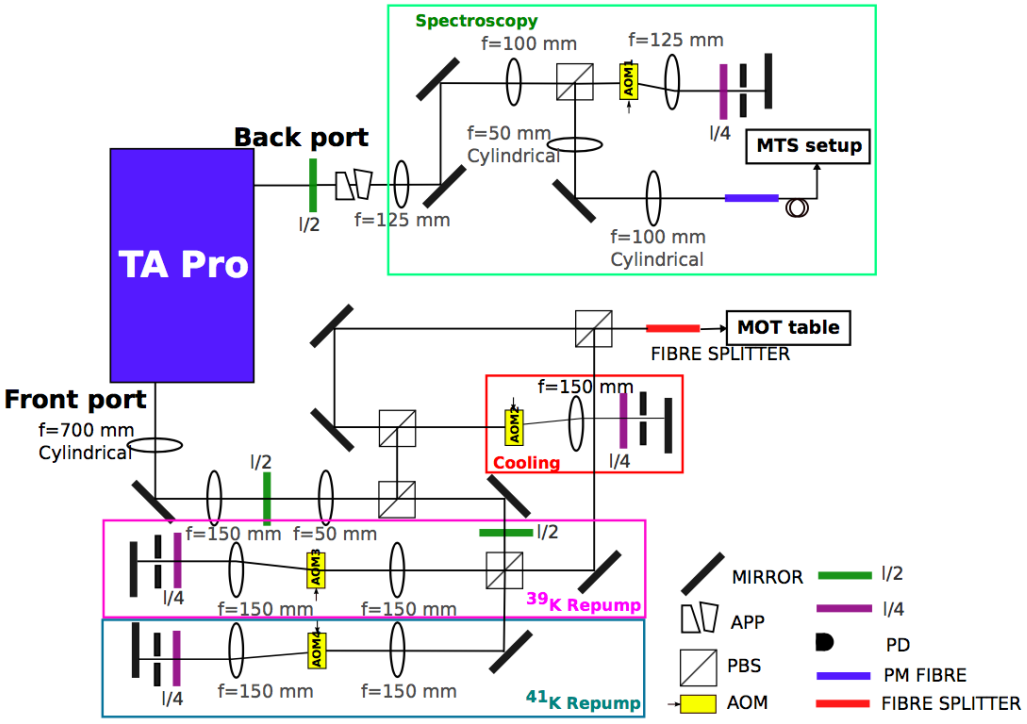


Figure 2.7: Schematic of the K laser setup.

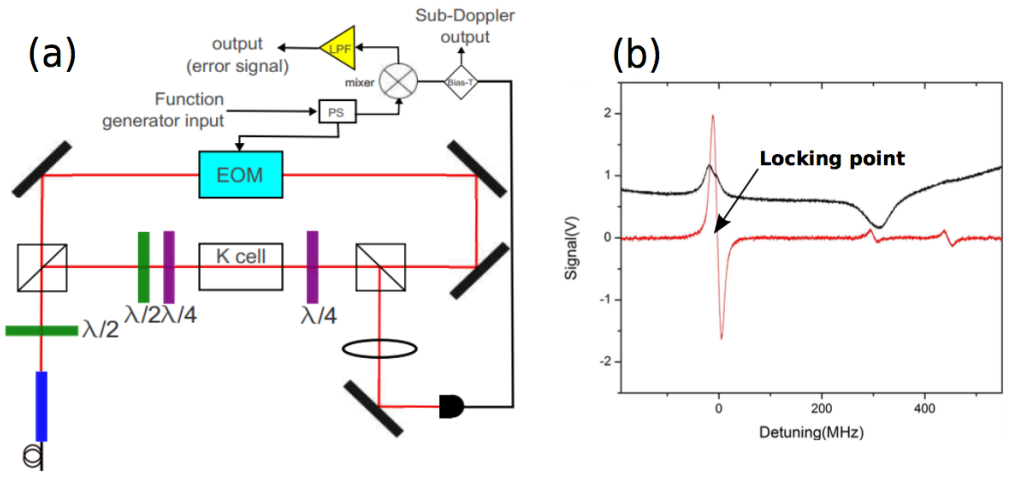


Figure 2.8: (a) Schematic of the modulation transfer spectroscopy (MTS), optics and electronics setup for laser stabilisation of potassium. (b) MTS error signal (red) together with its associated SAS signal (black) is shown.

tor F260APC-B. For K, the fibre collimator F810APC-842 together with a position-adjustable convex lense $f = 75$mm assembled in a cage system produce a beam with a waist of 6.3(6) mm on average. In the horizontal plane along $x$ and $y$ axis as shown in fig 2.1 the 852 nm and 767 nm beam paths are aligned independently. In the vertical plane along $z$ axis as shown in fig 2.1 both beams are aligned along the same path using a two-inch dichroic mirror, which provides 96.0% transmission for 767 nm and 95.8% reflection for 852 nm. Figure 2.9 presents the top-view of the arrangement, the vertical axis is not shown here.

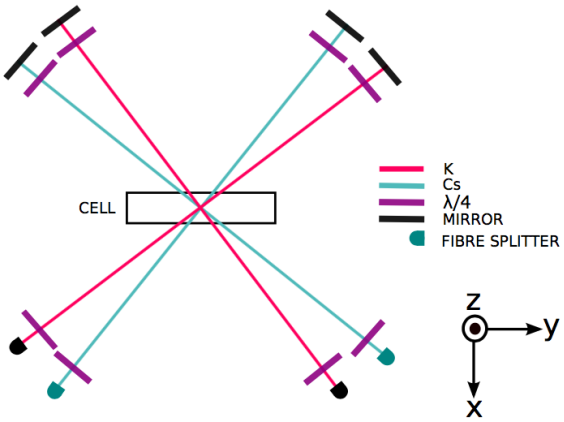


Figure 2.9: Schematic of the magneto-optical trap setup in the horizontal plane. K and Cs alignments are independent. It is basically three pairs of counter-propagating beams with the quarter waveplates to make all beams have circular polarisation.

## 2.4 Magnetic trap

There are five pairs of coils used at different stages of the experiment. In the MOT process two coils are needed. The quadrupole coils (green in fig 2.10) generate a quadrupole field with the gradient of 1.0(0) $\mathrm{G\,cm^{-1}A^{-1}}$. They are designed to trap atoms from the background vapour and also used as a magnetic trap. Three-axis shim coils are used for compensating the Earth's magnetic field. They provides uniform magnetic field in the Helmholtz configuration. Shim coils (shown in orange in fig 2.10) in the $z$-axis are assembled with other coils. To compensate stray fields along the $x-\&y$- axes, two parts

of shim coils are used (not shown in the figure). Fig 2.11 shows the shim X and Y calibration. The blue curves are generated by fitting to the equation of magnetic field on any axis perpendicular to the coil in the Helmholtz configuration described by [39] :

$$B_z = \frac{\mu_0}{2}\frac{NIR^2}{((z+s/2)^2+R^2)^{3/2}} + \frac{\mu_0}{2}\frac{NIR^2}{((z-s/2)^2+R^2)^{3/2}}, \tag{2.1}$$

where the Helmholtz pair consists of two coils of radius $R$, separated by a distance $s$ and $z$ is the axial distance from the centre of the coil. Each of the coil has $N$ turns and a current $I$ is flowing through in the same direction. The $\mu_0 = 4\pi \times 10^{-7}$ N A$^{-2}$ is the magnetic permeability of free space.

The properties of the shim coils are summarised in the table 2.1.

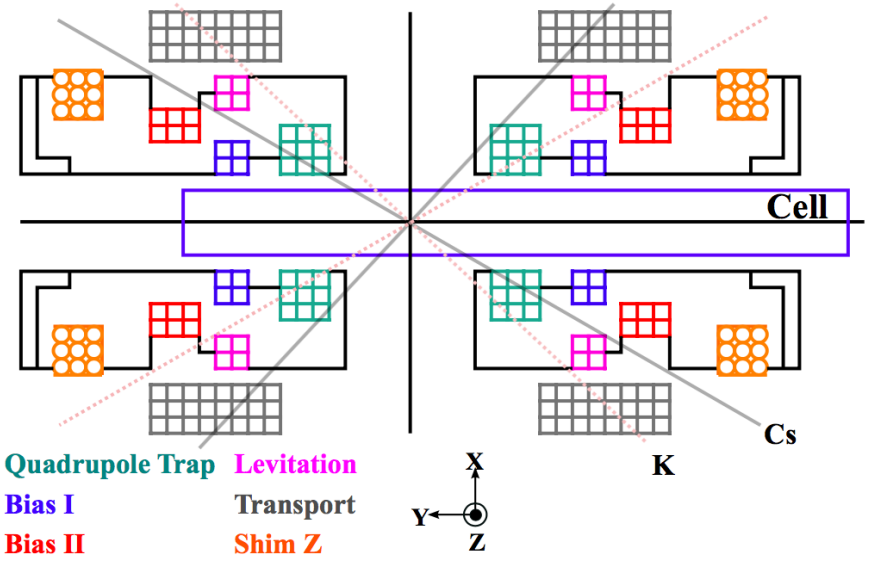


Figure 2.10: Cross-section of the coil assembly around the glass cell. Coils are in Helmholtz (Bias I, Bias II and Shim Z) and anti-Helmholtz (Quad, Levitation, Transport) configuration. The quadrupole coils are used for MOT and magnetic trapping in the evaporation stage. An additional bias field produced by Bias I Bias II might be used to accomplish efficient evaporation. Since we acquired the magnetic coil mount from our soliton experiment [39], there are other two coils in the mount (levitation and transport coils) not currently in use as we now run the experiment in a single chamber. In future, the setup will be more complicated and we might implement having two separated chambers, i.e., a MOT chamber and a science chamber and thus they are needed.

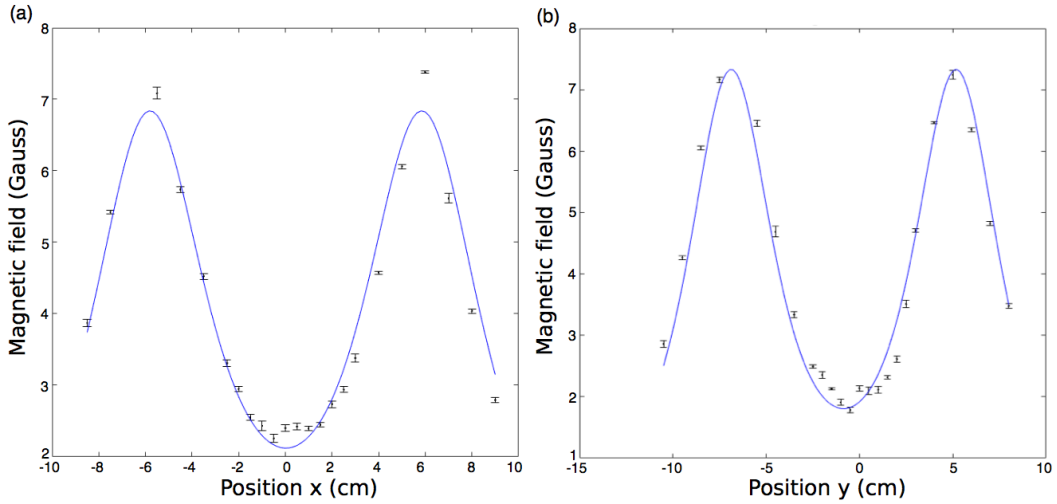


Figure 2.11: Calibration of shim coils along the $x$- and $y$- axis using a current of 2.(0) A. We measured the field four times and calculated an average and standard errors. The blue curves are fitted by the equation 2.1 for a pair of Helmholtz circular coils. For shim X(Y) it results in a radius of $r = 37.8$ (35.0) mm with a separation of $s = 117$ (121) mm.

| **Specification** | **shim X** | **shim Y** | **shim Z** |
|---|---|---|---|
| Width (mm) | 50(1) | 50(1) | 79(1) |
| Length (mm) | 50(1) | 50(1) | 79(1) |
| Inner separation (mm) | 117(1) | 117(1) | 35(1) |
| Outer separation (mm) | 134(1) | 134(1) | 100(1) |
| Number of turns | 20 | 20 | 44 |
| Field gradient ($\mathrm{G\,A^{-1}}$) | 1.2(5) | 1.0(5) | 6.2(1) |

Table 2.1: Measure specification of shim X, Y and Z coils.

Now we use quadrupole coils as MOT coils. In the MOT experiment the field at the centre of the MOT coils is supposed to be zero. However, the Earth's magnetic field causes the residual field of roughly 0.5 mG. In order to null the magnetic field with shim coils, the commercial magnetic sensor is used to probe it. It is a triple magnetometer HMC5883L from Honeywell company, which can measure the magnetic field up to 4 G with sensitivity of the order of a few mG. The probe is controlled by Arduino SMD A000073 interfaced with Labview so that the field can be real-time monitored. It is mounted on the nylon post holder to avoid additional stray magnetic fields.

## 2.5 Fluorescence imaging for diagnostics

The efficiency of the MOT stage can be quantified by the number of trapped atoms via different approaches such as fluorescence imaging and absorption imaging. The simplest way is the fluorescence imaging in which the fluorescence light emitted randomly from atoms is detected by a photodiode. For a linear detector the voltage signal from the photodiode is directly proportional to the trapped atom number. A MOT fluorescence signal captured within the solid angle of a convex lens with diameter 25.4 mm of a 40 mm focal length lens is focused on a photodiode (Thorlabs PDA100A-EC). The transverse magnification of the system is given by: $M_T = -s_i/s_o = 1.0$. The photodiode generates a current proportional to the fluorescence power incident on it with responsitivity $r(852\text{nm}) = 0.5(5)$ and $r(767\text{nm}) = 0.5(1)$ $\text{A W}^{-1}$. This current produces a voltage across a 2.3 MΩ oscilloscope input resistance which is proportional to atom number.

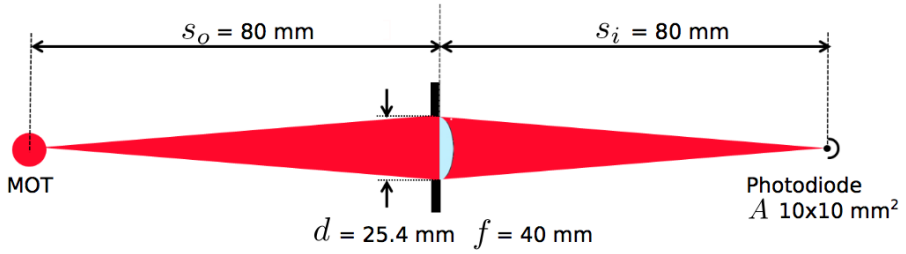


Figure 2.12: Schematic of one species fluorescence imaging. The imaging solid angle is limited by the lens by a 25.4 mm diameter aperture $d$ place at a distance $s_o$ from the MOT cloud. Currently, the detection is set up separately for two species, yet in the same configuration.

The fluorescence signal is related to the number of MOT atoms as follows. The power $P_{\text{total}}$ radiated by $N$ atoms illuminated by the laser of intensity is :

$$P_{\text{total}} = N \cdot \frac{hc}{\lambda} \cdot \Gamma_{\text{sc}} = N \cdot \frac{hc}{\lambda} \cdot \Gamma \frac{0.5 C_1 \frac{I_{\text{tot}}}{I_{\text{sat}}}}{(1 + C_2 \frac{I_{\text{tot}}}{I_{\text{sat}}} + 4(\frac{\Delta}{\Gamma})^2)}, \tag{2.2}$$

where $h$ is the Planck constant and $C_1, C_2$ ($C_1 = 0.7, C_2 = 0.73$ in our analysis) are the Townsend coefficient [40], which are determined from the fluorescence emission investigation, correcting for the fact that the MOT atoms are in an unknown distributed $m_F$ states. $I_{\text{tot}}$ is assumed to be six

times the single average beam intensity and $I_{\text{sat}} = 1.10$ (1.75) mW cm$^{-2}$ for Cs (K).

The power detected $P_{\text{det}}$ within the solid angle $\Omega$ limited by the convex lens [41]:

$$P_{\text{det}} = \frac{\Omega}{4\pi} \cdot P_{\text{total}} = \frac{1}{4\pi} \cdot \frac{\pi(d/2)^2}{s_o^2} \cdot P_{\text{total}} = \frac{d^2}{16 s_o^2} \cdot P_{\text{total}}, \tag{2.3}$$

incident on a photodiode of responsitivity $r(\lambda)$ produces a voltage across the oscilloscope terminal resistance R:

$$V_{\text{sig}} = I_{\text{sig}} \cdot R = r(\lambda) P_{\text{det}} \cdot R \tag{2.4}$$

Substituting $P_{\text{det}}$ and rearranging to obtain atom number as a function of the measured voltage:

$$N = V_{\text{sig}} \frac{16 s_o^2}{r R d^2} \frac{\lambda}{hc} \frac{2}{\Gamma} \frac{C_1 I_{\text{tot}} I_{\text{sat}}}{(1 + C_2 \frac{I_{\text{tot}}}{I_{\text{sat}}} + 4(\frac{\Delta}{\Gamma})^2)} \tag{2.5}$$

All parameters of Cs and K MOT are listed in the table 2.2.

| | $^{133}$**Cs** ($6^2\mathbf{S}_{1/2} \rightarrow 6^2P_{3/2}$) | $^{39}$**K** ($4^2\mathbf{S}_{1/2} \rightarrow 4^2\mathbf{P}_{3/2}$) | units |
|---|---|---|---|
| $I_{\text{tot}}$ | 6 $\times$53(1) | 6 $\times$ 25(1) | mW cm$^{-2}$ |
| $I_{\text{sat}}$ | 1.10(4) | 1.75(0) | mW cm$^{-2}$ |
| $\Delta$ | $2\pi \times -7.8(8)$ | $2\pi \times -18(1)$ | rad s$^{-1}$ |
| $s_0$ | 80(1) | 80(1) | mm |
| $d$ | 25.4(1) | 25.4(1) | mm |
| $r$ | 0.55(1) | 0.50(1) | A W$^{-1}$ |
| $R$ | 2.300 | 2.400 | M$\Omega$ |
| $N$ | 1.8(2) $\times 10^7$ | 3.2(9) $\times 10^7$ | Atoms |

Table 2.2: Experimental parameters for Cs and K fluorescence imaging.

Furthermore, not only a MOT loading curve derived from a fluorescence signal can indicate a saturated trapped atom number, the MOT loading rate and its lifetime can also be extracted from this curve. The loading rate as a function of $N$ trapped atoms is given by [22]:

$$\frac{dN}{dt} = L - \frac{N}{\tau}, \tag{2.6}$$

where $L$ is the loading rate, $\tau$ is the MOT lifetime that is inversely proportional to the loss rate ($\gamma = 1/\tau$) owing to collisions with background gas. Here the two-body light-assisted inelastic collisions between cold atoms is neglected due to low density in the MOT stage. Solving this equation, the number of trapped atoms as a function of time is characterised by:

$$N = L\tau(1 - e^{-t/\tau}). \tag{2.7}$$

To demonstrate this, fig 2.13, one of the $^{133}$Cs loading curves, is fitted to the equation 2.7. It shows that the atoms are captured at the rate 0.48(6) $\times 10^7$ atoms $\mathrm{s}^{-1}$ and the loss time is 1.6(9) s.

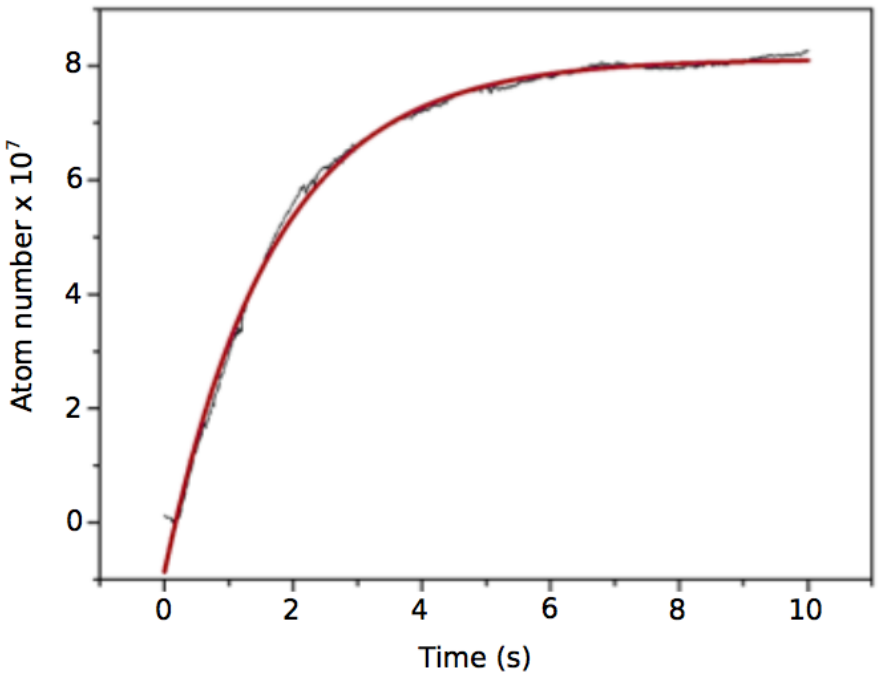


Figure 2.13: An example of the MOT loading curve for Cs. The black line is the number of trapped atoms calculated from the photodiode voltage of the fluorescence light. The data is best fit to the equation (2.7) as indicated as the red solid curve. We found that the atom loading rate ($L$) and the decay time ($\tau$) are 0.48(6) $\times 10^7$ atoms $\mathrm{s}^{-1}$ and 1.6(9) s respectively.

# Chapter 3

# Results and Discussions

This chapter describes the MOT optimisation of individual species, Cs and K respectively. In order to achieve the maximum number of atoms captured in the MOT, there are various parameters to be optimised which are dependent on one another. Those are the $\lambda/4$ waveplate angle, the null field position, the magnetic field gradient, the detuning of the cooling beam, the intensity of both the cooling and the repump beams, and the alkali vapour pressure via the dispenser current. We monitor the MOT using the camera and detect the fluorescence signals.

To start with, an optical alignment is tweaked until the beam crossing is at the position where the magnetic field is zero, i.e. the centre of the quadrupole coil. Secondly, thanks to the residual Earth's magnetic fields we ensure that the magnetic field gradient at the centre is null by applying additional constant fields to compensate it. They are produced by all three-axis shim coils characterised in section 2.4. The optimised shim fields result in the uniform free expansion of the MOT after switching the dispenser current off. Then, the angle of the $\lambda/4$ waveplates are all set correctly. In other words, the $\lambda/4$ waveplates are rotated in such a way that two horizontal beams become the circularly polarised light that drives the same transition. In contrast, ones for the vertical beam must be rotated in the opposite direction according to the direction of the quadrupole fields. After that, once all the setup has optimised the fluorescence signals, we start varying the detuning, the power, and the magnetic field gradient. Note that the dispenser current runs at 6 A

because the photodiode can detect a good amount fluorescence signal from 0.5 to 1 V corresponding to a significant number of atoms (on the order of $10^7$ sufficient for the later stages of the experiment).

## 3.1 Cs Optimisation

The MOT loading was investigated as a function of the intensity. The dispenser current is initially driven at 6 A and the MOT field gradient of 10.2(6) G cm$^{-1}$ is used. The cooling light is set to $2\pi\times7.8(8)$ MHz red-detuned from the cooling transition and the resonant repump light has the power of 0.6(2) mW per single beam. As can be seen in fig 3.1(a), the greater the power of the cooling light, the more atoms are trapped. We can trap on the order of $6 \times 10^7$ atoms. Eventually, we set the cooling light to maximum peak intensities of 6.5(1) mW cm$^{-2}$ for each beam.

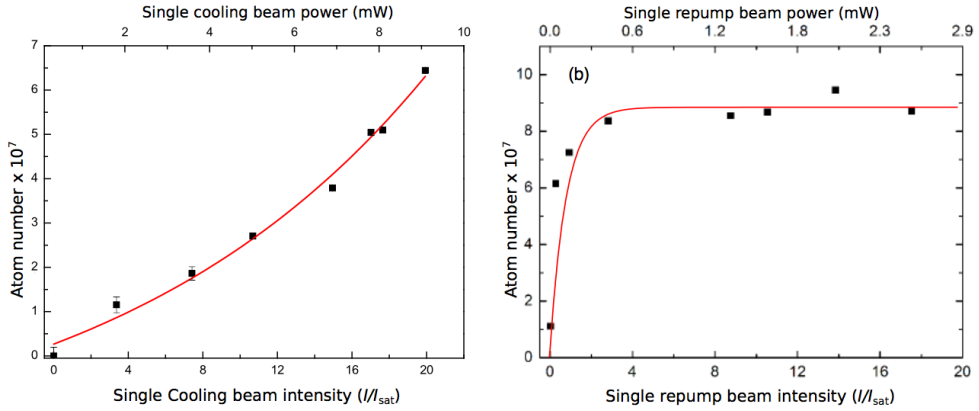


Figure 3.1: (a) Cooling light intensity optimisation of a Cs MOT. The black squares show the atom numbers at a given cooling beam intensity, whereas the red solid curve is a line to guide the eye showing the exponential growing. (b) repump light intensity optimisation for Cs.

The impact of the intensity of the repump laser is shown in fig 3.1 (b). The experiment is performed with the initial condition of the dispenser current, the MOT field gradient, the cooling light detuning as the cooling beam intensity investigation. Also, the cooling power is on average 9.0(6) mW per beam according to the first optimization of the cooling light intensity. From the plot, we can infer that the repump light provides at least 2.2(1) mW cm$^{-2}$ is sufficient to drive atoms back into the cooling cycles.

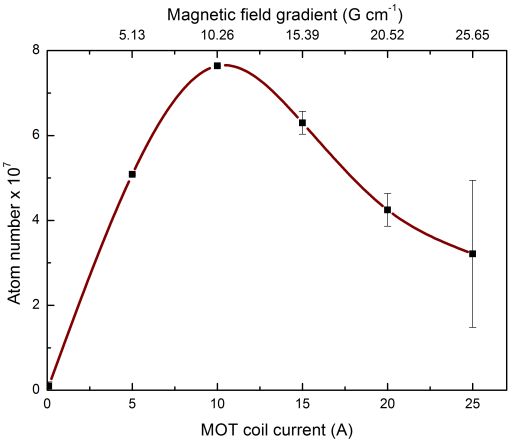


Figure 3.2: Dependence of the number of atoms trapped on the magnetic field gradient. We started to run the MOT coils at a low current of 5 A corresponding to the magnetic field gradient of 5.1(3) G cm$^{-1}$. The maximum number of atoms occurs at around 10 G cm$^{-1}$. The black squares are the data and the solid red line is a guide to show the trend of atom number at different magnetic fields. These data are taken with the cooling light detuning of 7.8(8) MHz and the single beam intensity of $19I_{\text{sat}}$.

The next parameter to consider is the magnetic field gradient associated with the trapping size and hence the MOT size. All parameters remain the same values ($P_{\text{cool}}$= 9.0(6) mW, $P_{\text{repump}}$ = 0.6(2) mW, $\Delta_{\text{cool}} = -2\pi \times 7.8(8)$ MHz), except the magnetic field. The experiment was performed by varying the current to the quadrupole coils from 5 to 25 A, corresponding to the approximate magnetic field gradients from 5 G cm$^{-1}$ up to 20 G cm$^{-1}$. In fig 3.2 it is apparent that as the magnetic field gradient increases, the number of captured atoms also rises until it reaches the optimum value and then falls down. From the fact that the Zeeman energy shift is proportional to the magnetic field gradient, as the position relative to the centre of the trap increases, the energy shift changes significantly. Therefore, the energetic atoms located further away from the trap centre hardly scatter with photons because it becomes far-off resonance to the cooling laser, and thus a smaller number of atoms are captured at higher magnetic field gradients. In addition, it can be observed that the MOT strongly depends on the detuning of the cooling beam as shown in fig 3.3. It also demonstrates the dependence between the field gradient and the cooling detuning. Finally, we can con-

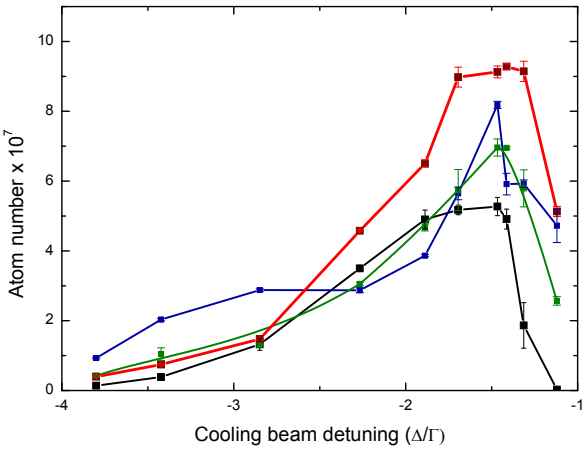


Figure 3.3: The cooling light detuning is varied for the magnetic field gradients of 5.1(3) G cm$^{-1}$ (black), 10.2(6) G cm$^{-1}$ (red) , 15.3(9) G cm$^{-1}$ (green) and 20.5(2) G cm$^{-1}$ (blue). The Cs atom numbers were measured via fluorescence detection. The graph shows the dependence between the detuning of the cooling beam and the magnetic field gradient. The working detuning is approximately 2Γ where the anti-Helmholtz coils runs at 10 A corresponding to gradient 10.2(6) G cm$^{-1}$.

clude that at the optimum magnetic field gradient of around 10.2(6) G cm$^{-1}$ the red-detuning of $2\pi\times7.8(8)$ MHz from resonance for $^{133}$Cs can trap the highest atom number up to $9.0(1)\times10^7$ can be achieved.

## 3.2 K Optimisation

For $^{39}$K, we are using the magnetic field gradient and dispenser current values that are optimum for a Cs MOT: 10.2(6) G cm$^{-1}$, 6 A respectively. We investigated the effect of varying the intensity and the detuning of the cooling light. We iteratively optimised the shim fields in such a way that both $^{39}$K and $^{133}$Cs MOT are loaded while maintaining the maximum number of atoms.

Unlike $^{133}$Cs, the hyperfine splittings of the $^{39}$K excited state as shown in fig 2.3 are small compared to its linewidth of the order of tens MHz leading to different behaviours of the cooling and the repump dependence. Consequently, the atoms cannot be purely driven on the cycling transition. In other words, off-resonance excitation is common. Figure 3.5(a) illustrates that by varying

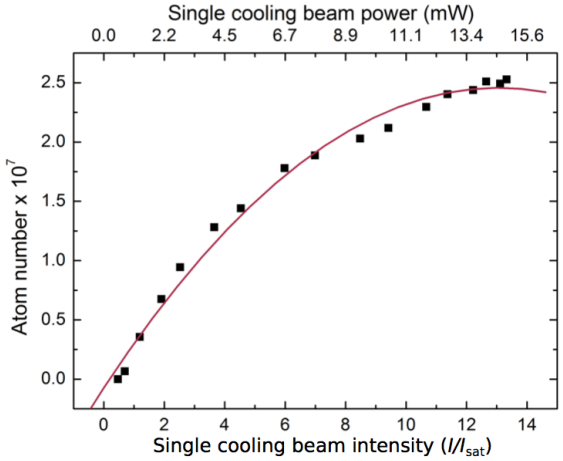


Figure 3.4: Optimisation of the cooling beam intensity for $^{39}$K. The cooling beam has been working at $14I_{\text{sat}}$ ($I_{\text{sat}}$ =1.75(0) mW cm$^{-2}$), which is the maximum intensity obtained from the laser system.

the cooling light detuning, the atom number has dropped within -4.5Γ and - 3.5Γ detuned from resonance and then increased. It might be because the laser frequency is resonant with the next hyperfine transition. Currently, the optimal detuning of the cooling at -$2\pi\times$18(1) MHz is set. This value is in accordance with the previous numerical study by [42] that Doppler cooling occurs in this region. At this detuning along with the repump detuning of $2\pi\times$15.0(1) MHz the number of atoms reaches an optimal value as shown in fig 3.5(b).

In conclusion, we can routinely start loading the $^{133}$Cs and $^{39}$K MOTs by setting laser powers, laser detunings, and the magnetic field to the following values as summarised in the table 3.1.

| **Parameters** | $^{133}$**Cs** | $^{39}$**K** | units |
|---|---|---|---|
| $\Delta_{\text{cooling}}$ | -7.8(8) | -18(1) | MHz |
| $\Delta_{\text{repump}}$ | 0.5(5) | 16(1) | MHz |
| $P_{\text{cooling}}$(per beam) | 9.0(6) | 22(1) | mW |
| $P_{\text{repump}}$(per beam) | 0.6(2) | 18.3(1) | mW |
| Magnetic field gradient | 10.2(6) | 10.7(7) | G cm$^{-1}$ |
| Typical atom number | 7(2) $\times10^7$ | 1(1) $\times10^7$ | Atoms |

Table 3.1: A summary table of optimised values of all parameters set in the MOT phase.

Once both species MOTs have been independently optimised, we investigate

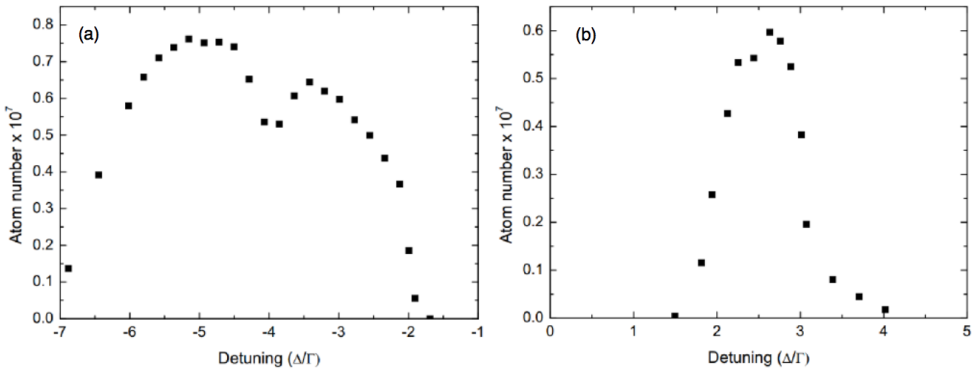


Figure 3.5: (a) Optimisation of the cooling beam detuning. $\Delta$ represents a detuning and the natural linewidth ($\Gamma$) of $D_2$ transition equals to $2\pi\times6.035$ MHz. The number of atoms is maximised at far red-detuned around 5 times of its linewidth. The atom number drops at $-4\Gamma$, where the laser frequency is far-off the cooling transition. (b) Optimisation of the repump beam detuning. The optimal repump detuning is approximately $2.5\Gamma$.

significant losses in one species in the presence of the other species as preliminarily illustrated in fig 3.6. Since the number of atoms in the $^{39}$K MOT is larger than of the $^{133}$Cs cloud, a roughly 4.7 % rapid reduction of $^{133}$Cs atom number is clearly observed when the $^{39}$K cloud is subsequently loaded after full $^{133}$Cs MOT loading for 1.5 s. This loss process in the two species MOT is caused by light assisted interspecies inelastic collisions [41]. For this reason the MOT parameters may need to be modified to reach the ideal performance, where it is allowed to load the two species MOT independently with the smallest reduction in atom number. The investigation of losses will help us to figure out how the inelastic collision losses can be suppressed.

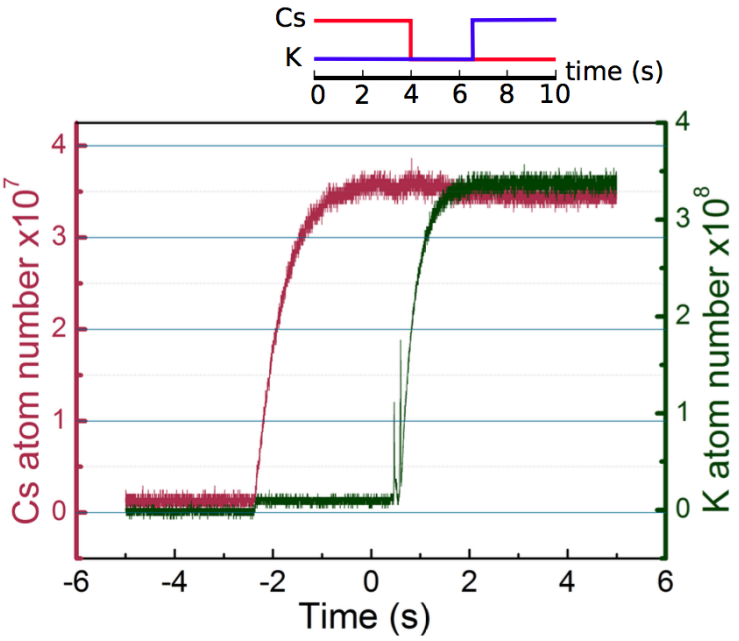


Figure 3.6: Loading and loss of $^{133}$Cs atoms. We initially trap only $^{133}$Cs atoms. After $\approx$ 2.5 s of $^{133}$Cs MOT loading, the cooling light and repump light of $^{39}$K are unblocked. It is clearly seen that the $^{133}$Cs trapped atoms are rapidly decaying by about 4.7 % of the fully loaded value when the $^{39}$K MOT is present.

# Chapter 4

# Conclusions and outlook

This thesis has contributed to MOT optimisation results for both $^{39}$K and $^{133}$Cs atoms. Significant optimised parameters are summarised in section 4.1 and an outlook towards future work on the experiment is discussed in section 4.2.

## 4.1 Summary

During this thesis we have developed an understanding and experimental skills about laser systems and MOT setup as well as techniques of laser stabilisation necessary in ultracold gases experiments. My work is to investigate the effect of laser detuning, MOT beam intensity and the magnetic field gradient of the quadrupole field on the number of individual $^{39}$K and $^{133}$Cs atoms collected via the MOT technique. The experimental results indicates that all parameters are dependent upon one another. To summarise, at an optimisation stage the vapour dispenser of both species is continuously run at the current of 6 A providing sufficient background vapour for the collection of atoms in the MOT. The optimum magnetic field gradient is around 10 $\mathrm{G\,cm^{-1}}$. For $^{39}$K, we can trap $2.5(1) \times 10^7$ atoms by using the cooling detuning at $-5\Gamma$ with the intensity of $14I_{\mathrm{sat}}$ and the repump detuning at $2.5\Gamma$, where $I_{\mathrm{sat}}$ is the saturation intensity having a value of $1.75(0)$ $\mathrm{mW\,cm^{-2}}$ and $\Gamma$ is the natural linewidth of the excited state equal to $2\pi\times$ 6.03(5) MHz. In the case of $^{133}$Cs, the atom number can be maximised up to $7(2) \times 10^7$ in

our MOT. This is achieved by using the -1.5Γ detuned cooling light with a single beam intensity of $20I_{\text{sat}}$ and the resonant repump light with the intensity around the saturation intensity, where $\Gamma = 2\pi \times 5.234$ MHz and $I_{\text{sat}} = 1.10(4)\ \text{mW}\,\text{cm}^{-2}$.

## 4.2 Project Outlook

Once both $^{39}$K and $^{133}$Cs MOT are optimised, the atoms will be loaded into a magnetic trap for evaporation. By doing so efficiently, optical molasses and cMOT are performed and followed by optical pumping to the magnetically trapped state in a magnetic trap. The forced evaporative cooling using radio frequency (RF) is exploited to cool atoms further. However, the cooling process is ceased near the centre of the trap due to Majorana losses causing spin-flip towards untrapped states. Following this the atoms are loaded into an optical dipole trap. By decreasing the trap depth associated with reduction of the dipole trap power, atoms can rethermalise to a lower temperature. This stage takes advantage of magnetic moment quantum number independence and thus all states can be optically trapped.

Furthermore, the idea of pulsing the dispenser instead of running continuously need to be revisited. The current, the pulse duration and the time lag between pulses will be optimised by observing the evolution of the modulated vapour pressure in a single cell when turning the dispenser on and off and see how all parameters have an impact on the MOT lifetime.

After both species reach the degeneracy, Feshbach resonance spectroscopy of individual $^{39}$K and $^{133}$Cs will be investigated in order to understand the scattering properties of them. Additionally, interspecies Feshbach resonances of $^{39}$K$^{133}$Cs will be located when the ultracold mixtures of $^{39}$K and $^{133}$Cs is produced.
Another prospect of ultracold $^{39}$K and $^{133}$Cs molecules production is via optical tweezers. This technique offers a single molecule formation and realisation of small molecules array by controlling molecule-molecule interaction. It also provides the possibility to study surface science by bringing molecules close

to the surface and inducing the strong coupling.

The idea is to demonstrate single atom of $^{39}$K and $^{133}$Cs loading of separated optical tweezers. Then, overlap the tweezers and associate them into a single molecule. This approach is adventurous that the atomic samples are not necessary cold as one loading in optical lattices, resulting in the reduction of timing sequence. More importantly, we can perform the experiment in our current apparatus.

The combination of magneto association and STIRAP has been proved to successfully prepare ultracold polar ground state molecules such as $^{40}$K$^{87}$Rb and $^{87}$RbCs. This work makes the possibility to create another species that are bosonic $^{39}$K and $^{133}$Cs and maybe fermionic $^{41}$K and $^{133}$Cs molecules. Thanks to the fact that they are inactive against reactions, it opens a window to be able to manipulate them to explore exciting aspects in fundamental physics as we proposed to use them simulate condensed-matter problems.

# Bibliography


[1] A. Pikovski, M. Klawunn, G. V. Shlyapnikov, and L. Santos, *Interlayer Superfluidity in Bilayer Systems of Fermionic Polar Molecules*, Phys. Rev. Lett. **105**, 215302 (2010).

[2] K. G. T. Köhler and P. S. Julienne, *Production of cold molecules via magnetically tunable Feshbach resonances*, Rev. Mod. Phys. **78**, 1311 (2006).

[3] M. A. Baranov, A. Micheli, S. Ronen, and P. Zoller, *Bilayer superfluidity of fermionic polar molecules: Many-body effects*, Phys. Rev. A **83**, 043602 (2011).

[4] K. M. Evenson, J. S. Wells, F. R. Petersen, B. L. Danielson, and G. W. Day, *Speed of light from direct frequency and wavelength measurement of the methane-stabilized laser*, Phys. Rev. Lett. **29**, 1346 (1972).

[5] L. M. Barnett R, Petrov D and D. E, *Quantum magnetism with multicomponent dipolar molecules in an optical lattice*, Phys. Rev. Lett. **96**, 190401 (2006).

[6] I. Bloch, J. Dalibard, and S. Nascimbene, *Quantum simulations with ultracold quantum gases*, Nature Physics **42**, 267 (2012).

[7] A. Micheli, G. Brennen, and P. Zolle, *A toolbox for lattice-spin models with polar molecules*, Nature Physics **2**, 341 (2006).

[8] A. V. Gorshkov *et al.*, *Tunable Superfluidity and Quantum Magnetism with Ultracold Polar Molecules*, Phys. Rev. Lett. **107**, 115301 (2011).

[9] M. Greiner, O. Mandel, T. Esslinger, T. Hänsch, and I. Bloch, *Quantum phase transition from a superfluid to a Mott insulator in a gas of ultracold atoms*, Nature **415**, 39 (2002).

[10] C. Regal and D. Jin, *Experimental Realization of the BCS-BEC Crossover with a Fermi Gas of Atoms*, Adv. At. Mol. Opt. Phy. **54**, 1 (2007).

[11] M. Inguscio and L. Fallani, *Atomic Physics: Precise Measurements and Ultracold Matter*, First ed. (Oxford Scholarship Press, 2013).

[12] N. R. Cooper and G. V. Shlyapnikov, *Stable Topological Superfluid Phase of Ultracold Polar Fermionic Molecules*, Phys. Rev. Lett. **103**, 155302 (2009).

[13] P. K. Molony, *Creation of Ultracold* $^{87}Rb$ $^{133}Cs$ *Molecules in the Rovibrational Ground State*, Phys. Rev. Lett. **113**, 255301 (2014).

[14] S. Ni K-K Ospelkaus *et al.*, *A high phase-space-density gas of polar molecules*, Science **322**, 231 (2008).

[15] T. Tiecke, *Properties of potassium*, PhD thesis, University of Amsterdam, The Netherlands, 2010.

[16] H. J. Patel, C. L. Blackley, S. L. Cornish, and J. M. Hutson, *Feshbach resonances, molecular bound states, and prospects of ultracold-molecule formation in mixtures of ultracold K and Cs*, Phys. Rev. A **90**, 032716 (2014).

[17] V. Dugrain, P. Rosenbusch, and J. Reichel, *Alkali vapor pressure modulation on the 100 ms scale in a single-cell vacuum system for cold atom experiments*, Rev. Sci. Instrum. **85** (2014).

[18] J. Hutson and P. Soldán, *Molecule formation in ultracold atomic gases*, Int. Rev. in Phys Chem **25**, 497 (2006).

[19] T. Wall *et al.*, *Stark deceleration of CaF molecules in strong- and weak-field seeking states*, Phys. Chem. Chem. Phys. **13**, 18991 (2011).

[20] J. Lim, M. D. Frye, J. M. Hutson, and M. R. Tarbutt, *Modeling sympathetic cooling of molecules by ultracold atoms*, Phys, Rev. A **92**, 053419 (2015).

[21] W. D. Phillips, *Laser Cooling and Trapping of Neutral Atoms*, Rev. Mod. Phys. **70** (1998).

[22] H. Metcalf and P. van der Straten, *Laser Cooling and Trapping*, First ed. (Springer, 1999).

[23] N. R. Hutzler, H.-I. Lu, and J. M. Doyle, *The buffer gas beam: an intense, cold, and slow source for atoms and molecules*, Chem. Rev **112**, 4803 (2012).

[24] K. M. Jones, E.Tiesinga, P. D. Lett, and P. Julienne, *Ultracold photoassociation spectroscopy: Long-range molecules and atomic scattering*, Rev. Mod. Phys. **78**, 483 (2006).

[25] K. Bergmann, H. Theuer, and B. Shore, *Coherent population transfer among quantum states of atoms and molecules*, Rev. Mod. Phys. **70**, 1003 (1998).

[26] I. G. Hughes and M. J. Pritchard, *Cool things to do with lasers*, Phys. Educ. **42**, 29 (2007).

[27] *Cooling and Trapping Techniques with Ultracold Atoms*, 2009.

[28] D. A. Steck, *Cesium D Line Data*, (1998).

[29] W. H. Wing, *On neutral particle trapping in quasistatic electromagnetic fields*, Prog. Quant. Elec **8**, 181 (1984).

[30] C. J. Foot, *Atomic Physics*, First ed. (Oxford University Press, 2005).

[31] T. Weber, J. Herbig, , N. N.C., and R. Grimm, *Three- Body Recombination at Large Scattering Lengths in an Ultracold Atomic Gas*, Phys. Rev. Lett. **91**, 123201 (2003).

[32] T. Weber, J. Herbig, M. Mark, H.-C. Nägerl, and R. Grimm, *Bose-Einstein Condensation of Cesium*, Science **299**, 232 (2003).

[33] M. P. Köppinger, *Creation of ultracold RbCs molecules*, PhD thesis, Durham University, UK, 2014.

[34] D. J. McCarron, *A Quantum Degenerate Mixture of RbCs*, PhD thesis, Durham University, UK, 2011.

[35] S. A. Moses, J. P. Covey, M. T. Miecnikowski, D. S. Jin, and J. Ye, *New frontiers for quantum gases of polar molecules*, Nat Phys **advance online publication**, (2016).

[36] T. G. Tiecke, *Properties of potassium*, PhD thesis, University of Amsterdam, 2010.

[37] K. MacAdam, A. Steinbach, and C. Wieman, *A narrow-band tunable diode laser system with grating feedback, and a saturated absorption spectrometer for Cs and Rb*, American Journal of Physics **60**, 1098 (1992).

[38] D. J. McCarron, S. A. King, and S. L. Cornish, *Modulation transfer spectroscopy in atomic rubidium*, Measurement science and technology **19**, 105601 (2008).

[39] S. Händel, *Experiments on ultracold quantum gases of 85Rb and 87Rb*, PhD thesis, Durham University, UK, 2011.

[40] C. G. Townsend *et al.*, *Phase-space density in the magneto-optical trap*, Phys. Rev. A **52**, 1423 (1995).

[41] P. Tierney, *Magnetic Trapping of an Ultracold 87Rb -133Cs Atomic Mixture*, PhD thesis, Durham University, UK, 2009.

[42] M. Landini *et al.*, *Sub-Doppler laser cooling of potassium atoms*, Phys. Rev. A **84**, 043432 (2011).